

Cite this: *Soft Matter*, 2012, **8**, 9183

www.rsc.org/softmatter

PAPER

Macroscopically oriented hierarchical structure of the amphiphilic tetrathiafulvalene molecule†

Namil Kim,^{‡a} Lei Wang,^{‡b} Dae-Yoon Kim,^c Seok-Ho Hwang,^d Shiao-Wei Kuo,^e Myong-Hoon Lee^{*c} and Kwang-Un Jeong^{*c}

Received 4th May 2012, Accepted 29th June 2012

DOI: 10.1039/c2sm26458g

Since the physical properties of electronic and biological molecules strongly depend on the nature of molecular self-assembly and organization, it is essential to control their molecular packing structure and morphology on the different length scales. In this aspect, a programmed amphiphilic tetrathiafulvalene (TTF) molecule (abbreviated as amph-7TTF14) was newly designed and synthesized. Differential scanning calorimetry (DSC) combined with one-dimensional (1D) wide angle X-ray diffraction (WAXD) techniques revealed that a highly ordered crystalline phase emerged below the isotropic phase. From the 2D WAXD pattern of the macroscopically oriented amph-7TTF14 film, the crystal structure was identified to be a monoclinic unit cell. The face-to-face π - π interaction between TTF groups and the nanophase separation between rigid TTF groups and flexible hydrophobic alkyl and hydrophilic tri(ethylene oxide) tails were the main driving forces for the self-assembly of amph-7TTF14. The morphological observations using transmission electron microscopy (TEM), atomic force microscopy (AFM), and polarized optical microscopy (POM) indicated that the amph-7TTF14 formed not only flat ribbons but also scrolls and helices, in which the ribbons further aggregated to create the fibrous hierarchical structures. Based on the experimental results and careful analyses, it was realized that the scrolls and helices were induced by the unbalanced surface stresses generated during the crystallization process. When the macroscopically oriented fibrous hierarchical structure is properly applied to the electrooptical and bio-mimetic devices, the targeted physical properties may be significantly improved and tuned for the specific practical applications.

Introduction

Self-assembly is a spontaneous molecular organization process utilizing the programmed physical interactions, such as hydrogen bonding, electrostatic (ion-ion, ion-dipole, and dipole-dipole) interaction, π -orbital overlapping, van der Waals interaction, and hydrophobic-hydrophilic effects, along with the possible involvement of growth kinetics.¹⁻⁷ Formation of hierarchical

architectures from biological molecules on the different length scales may be a good example of self-assembly.⁸⁻¹⁶ Most biomaterials possess atomic configurational chirality (the primary chirality) on the sub-nanometer scale, which makes them integrate the biological information in the limited space.⁸⁻¹⁶ Through the noncovalent interactions, the configurational chirality of the chemical structures often forces them to form helical conformers (the secondary chirality) on a nanometer scale.⁸⁻¹⁶ The nonparallel and cooperative packing of the helical conformers can result in the formation of phase chirality (the tertiary chirality) on a micrometer scale.⁸⁻¹⁶ Finally, the phase structures further aggregate to form object chirality (the quaternary chirality) on a macroscopic micrometer length scale.⁸⁻¹⁶

The design and synthesis of chiral molecules as well as the control of chirality transfer on the length scale from sub-nanometer to micrometer are critical for the achievement of macroscopic properties desired for specific bio-mimetic and optical applications. Through the systematic research, scientists and molecular engineers have realized that, without establishing the links for the chiral transfer across the hierarchical length scale, it is impossible to correlate the primary, the secondary, the tertiary and the quaternary chiralities.¹⁷⁻²¹ Recently, it was reported that

^aKorea Automotive Technology Institute, Cheonan 330-912, Korea

^bNational Centre for Nanoscience and Technology, Beijing 100190, China

^cDepartment of Polymer-Nano Science and Technology and Department of Flexible and Printable Electronics, Chonbuk National University, Jeonju 561-756, Korea. E-mail: kujeong@jbnu.ac.kr; mhlee2@jbnu.ac.kr; Fax: +82 63 270 2341; Tel: +82 63 270 4633

^dDepartment of Polymer Science and Engineering, Dankook University, Yongin 448-701, Korea

^eDepartment of Materials Science and Optoelectronic Engineering, National Sun Yat-Sen University, Kaohsiung 804, Taiwan

† Electronic supplementary information (ESI) available: ¹H and ¹³C NMR, UV-Vis, SAED and CV results and synthetic processes of the amph-7TTF14 compound are represented and discussed. See DOI: 10.1039/c2sm26458g

‡ These authors contributed equally to this work.

a series of specifically designed chiral polyesters [PET-(R*)-*n*, where *n* is the number of methylene units; *n* = 7–11] formed helical single crystals.^{22–30} Based on the systematic experiments and careful analyses, it was realized that the handedness of the helical sense was determined by the configurational chirality as well as by the number of methylene units.^{22–30} Therefore, configurational chirality is not necessary requirement for the formation of hierarchical chiralities. A parallel and noncooperative molecular packing blocks the chiral transfer from the primary/secondary chirality to the tertiary chirality.^{22–30} On the other hand, as reported in the polyethylene twisted lamellae crystals, phase chirality originates from a collective tilt of the achiral molecules with respect to the layer normal.^{22–30} The formation of phase chirality from achiral molecules is mainly driven by the unbalanced surface stresses generated between the two lamellar basal surfaces. Faster growth on the one side of the growth plane (kinetic effect) could be another reason.^{31–37}

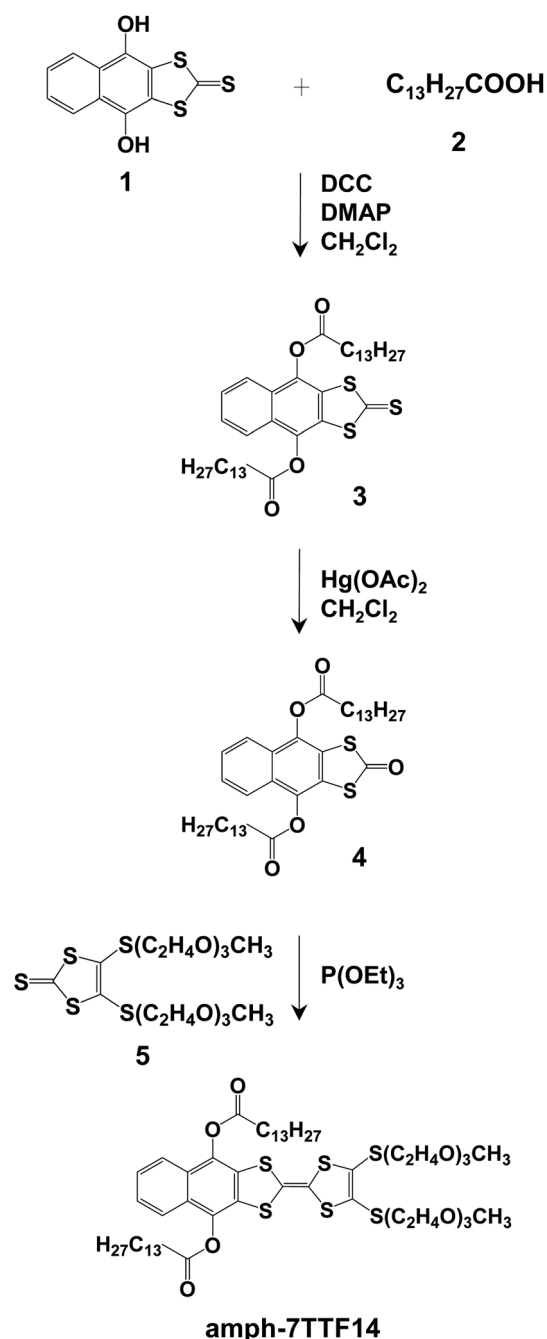
Recently, we reported a series of swallow-shaped asymmetric tetrathiafulvalene (TTF) molecules (a-6TTF12) which reveal a highly ordered columnar liquid crystalline (Φ_{LC}) phase and a columnar crystalline (Φ_{CT}) phase with a monoclinic unit cell as descending temperatures.³⁸ There were two main driving forces in the formation of the ordered columnar phases. One was the π - π interaction among the TTF-based mesogens, causing $I \leftrightarrow \Phi_{LC}$ phase transition, and the other was the nanophase separation between the rigid TTF-based mesogens and the flexible alkyl chains. The formation of a highly ordered columnar Φ_{LC} phase at room temperature may be promising for organic optoelectronic devices, since the self-organization of LC molecules allows us to control the macroscopic alignment of molecules and to minimize the defects.³⁸

In this research, we newly designed and synthesized an asymmetric amphiphilic TTF molecule (amph-7TTF14) by covalently connecting two tri(ethylene oxide) (TEO) tails at both sides of the TTF group and two alkyl tails with 14 carbon atoms at one end of the TTF group. Phase behavior of amph-7TTF14 was studied by combined techniques of differential scanning calorimetry (DSC) and one-dimensional (1D) wide angle X-ray diffraction (WAXD). The ordered molecular packing was identified from the 2D WAXD pattern, and its molecular arrangement was confirmed by selected area electron diffraction (SAED) and polarized ultraviolet-visible (UV-Vis) spectroscopy. The molecular arrangements in the flat ribbons, scrolls and helices were investigated by SAED and cross-polarized optical microscopy (POM) with a retardation film. Furthermore, the optical and electrochemical properties of amph-7TTF14 were studied using UV-Vis spectroscopy and cyclic voltammetry.

Results and discussion

Programmed amphiphilic tetrathiafulvalene molecule and its thermal properties of phase transformation

As illustrated in Scheme 1, an asymmetric amphiphilic tetrathiafulvalene (TTF) molecule having two tri(ethylene oxide) (TEO) tails at both sides of the TTF moiety and two alkyl tails with 14 carbon atoms at one end of the TTF moiety was designed and synthesized *via* two-step reactions: an esterification reaction in the presence of 1,3-dicyclohexyl carbodiimide (DCC)/



Scheme 1

4-dimethylaminopyridine (DMAP) followed by a phosphate-induced cross-coupling reaction. The asymmetric amphiphilic TTF molecule was abbreviated as amph-7TTF14. Here, 7 and 14 stand for the number of carbons in the TEO and alkyl tails, respectively. In the amph-7TTF14 chemical structure, the electron withdrawing ester linkage was purposely adopted to increase the air/light stability by decreasing the highest occupied molecular orbital (HOMO) level.^{39,40} In Scheme 1, the cross-coupling reaction of **5** with excess of **4** in P(OEt)₃ at 120 °C for 4 h yielded an asymmetric mesogenic core structure of amph-7TTF14. The amph-7TTF14 compound was extensively purified by column chromatography several times. The chemical

structure and purity were confirmed by proton (^1H) and carbon-13 (^{13}C) nuclear magnetic resonance (NMR) spectroscopies, as represented in Fig. S1 and S2 in the ESI.†

The molecular weight of amph-7TTF14 is 1113.7 g mol^{-1} . The molecular dimensions and minimal energy geometry of amph-7TTF14 in the isolated gas phase were estimated by utilizing Cerius² (version 4.6) computer simulation software from Accelrys. The results are represented in Fig. 1c–e: front- (xy -plane), side- (yz -plane) and top-view (xz -plane), respectively. The calculated core length of amph-7TTF14 along the y -axis is 1.36 nm, while the width of the core along the x -axis is 0.51 nm, as shown in Fig. 1d and e. Assuming the all-*trans* conformation in the alkyl and TEO chains, the length of amph-7TTF14 is 2.36 nm along the y -axis, and its width is 4.12 nm along the x -axis. The amph-7TTF14 compound is also schematically depicted in Fig. 1b in order to emphasize the fact that amph-7TTF14 consists of the hydrophilic/hydrophobic flexible tails and aromatic rigid core.

To determine the thermal transition temperature and quantitative thermodynamic properties of the amph-7TTF14 compound, DSC experiment was first conducted. As shown in Fig. 2, DSC thermograms exhibit a single exothermic peak at different cooling rates from 2.5 to $40\text{ }^\circ\text{C min}^{-1}$ in the investigated temperature range. Upon increasing the cooling rate, the onset temperature shifts to lower temperatures and the heat (ΔH) release at transition is reduced. At the $2.5\text{ }^\circ\text{C min}^{-1}$ cooling rate, the onset temperature of the exothermic transition and corresponding heat are $33.3\text{ }^\circ\text{C}$ and 58.4 J g^{-1} (65.0 kJ mol^{-1}), which are reduced to $25.4\text{ }^\circ\text{C}$ and 50.0 J g^{-1} (55.7 kJ mol^{-1}) at $20\text{ }^\circ\text{C min}^{-1}$. From the linear dependence on the cooling rate, the onset transition temperature and heat at equilibrium are estimated to be $34.5\text{ }^\circ\text{C}$ and 59.5 J g^{-1} (66.3 kJ mol^{-1}), respectively. The variation of the transition temperature depending on the cooling

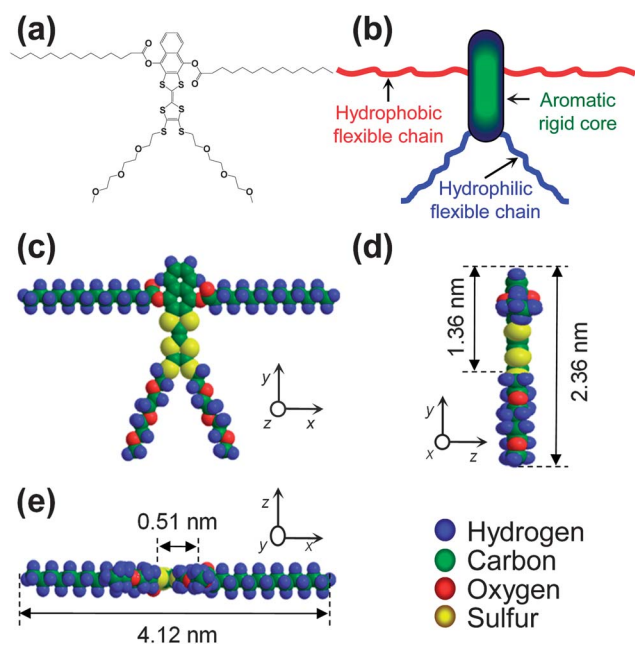


Fig. 1 Chemical structure (a) and schematic illustration (b) of amph-7TTF14. Calculated geometric dimensions of the molecule in the views from the z -axis (c), x -axis (d), and y -axis (e), respectively.

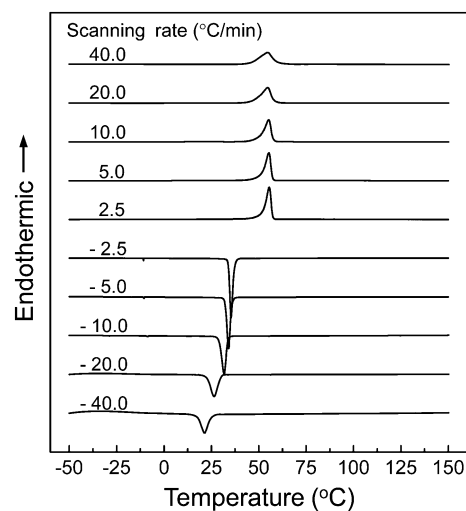


Fig. 2 Sets of DSC cooling and subsequent heating thermal diagrams for amph-7TTF14 at scanning rates ranging from 2.5 to $40\text{ }^\circ\text{C min}^{-1}$.

rate implies that the heat is associated with crystallization.^{41–54} Hence, the endothermic thermal transition detected upon subsequent heating is ascribed to the crystal melting. The thermodynamic properties obtained from the subsequent heating process are consistent with those from the cooling process.

Although the DSC technique is sensitive to heat absorption and release events at thermal transitions and serves quantitative thermodynamic properties, it does not provide direct information regarding the molecular ordering at transitions.^{41–55} 1D WAXD was used to investigate the temperature-dependent structural development of amph-7TTF14. Fig. 3 shows a set of 1D WAXD patterns of the amph-7TTF14 compound obtained at a cooling rate of $2.5\text{ }^\circ\text{C min}^{-1}$. It is apparent that phase transition takes place when temperature reaches $35\text{ }^\circ\text{C}$, which agrees well with crystallization behavior in DSC (Fig. 2). Above $35\text{ }^\circ\text{C}$, the amph-7TTF14 molecules are in the isotropic state (I), exhibiting only two amorphous halos at $2\theta = 4.60^\circ$ (d -spacing

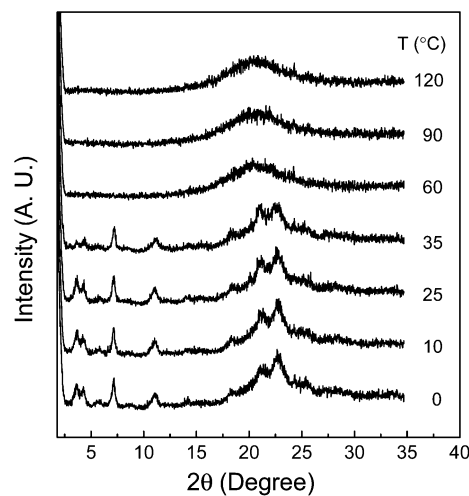


Fig. 3 (a) Sets of 1D WAXD powder patterns of amph-7TTF14 molecule obtained at different temperatures between 0 and $120\text{ }^\circ\text{C}$ during cooling at a rate of $2.5\text{ }^\circ\text{C min}^{-1}$.

1.92 nm) and $2\theta = 20.7^\circ$ (d -spacing = 0.43 nm) which correspond to the average periodicity of electron density fluctuations between the nanophase separated TTF cores and alkyl tails and to the average distance among the amorphous chains, respectively. At 35°C , many sharp reflection peaks suddenly appeared in both low and wide angle regions, signifying that the highly ordered crystals emerged. Note that the corresponding asymmetric tetrathiafulvalene molecules containing only hydrophobic alkyl chains both at the side and at the end of the TTF mesogen revealed not only a columnar crystalline phase with a monoclinic unit cell but also a highly ordered columnar liquid crystalline phase.^{38,56}

Identification of molecular packing structures

Since DSC and 1D WAXD techniques are not suitable to provide the detailed structural and symmetrical information,⁴⁹ the 2D WAXD and SAED experiments were carried out. The oriented sample was prepared by mechanical shearing just below the onset crystallization temperature (35°C). Fig. 4 shows the 2D WAXD pattern of an oriented amph-7TTF14 at 30°C . The incident X-ray beam direction is normal to the shear direction (the SD along the meridian). The diffractions are observed on the equator and meridian as well as in the quadrants, implying that the sample possesses the 3D ordered crystalline phase.

As described in Fig. 4, the a^* and b^* axes are located on the equator, while the c^* -axis is parallel to the meridian direction (SD). It is a typical X-ray fiber pattern of the uniaxially oriented fiber. On the equator, there are three distinct diffractions at low 2θ -angle region close to the X-ray beam stop, *i.e.*, $2\theta = 3.70, 4.10$ and 5.71° , with corresponding d -spacings of 2.39, 2.15 and 1.55 nm. Based on the triangulation method of building a 2D a^*b^* lattice of the unit cell and the consideration of packing structure of asymmetric amph-7TTF14 compound,⁵⁶ these diffractions correspond to the (100), (020), and (120) plane accordingly. A series of relatively weak diffractions on the equator between $2\theta = 7.40^\circ$ (d -spacing = 1.19 nm) and 11.11°

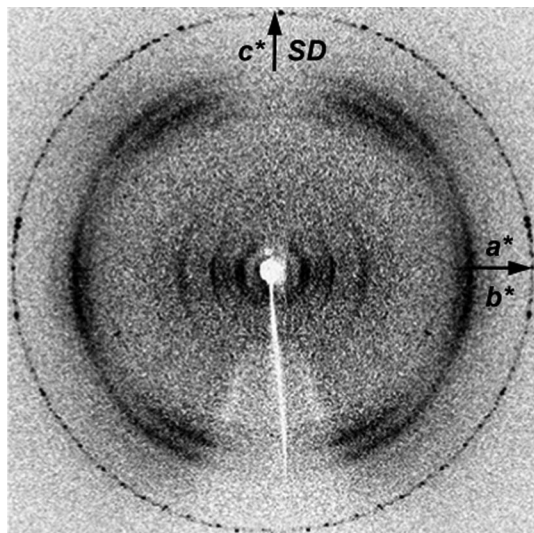


Fig. 4 2D WAXD pattern of the columnar crystalline Φ_K phase of amph-7TTF14 at room temperature.

(d -spacing = 0.80 nm) fit well with the 2D a^*b^* lattice. Through the refinement of the reciprocal 2D a^*b^* lattice using the diffractions on the equator, a real space 2D unit cell is evaluated with dimensions of $a = 2.39$ nm, $b = 4.32$ nm, and $\gamma = 94^\circ$.

A pair of relatively diffused diffraction arcs at $2\theta = 18.5^\circ$ (d -spacing = 0.480 nm) on the meridian (along the c^* -axis) is identified as the (001) plane. This assignment is further supported by a series of diffractions of the first layer ($hk1$) of the 2D WAXD pattern. The ($hk1$) diffractions at $2\theta = 18.86^\circ$ (d -spacing = 0.471 nm), 19.4° (d -spacing = 0.458 nm), 19.9° (d -spacing = 0.445 nm), 20.7° (d -spacing = 0.429 nm), 21.7° (d -spacing = 0.411 nm), 22.9° (d -spacing = 0.388 nm) and 23.8° (d -spacing = 0.374 nm) correspond to the Miller indices of (101), (121), (201), (141), (301), ($\bar{3}41$) and (401), respectively. Because the (001) diffraction is on the meridian and the a^* and b^* axes are along the equator, the dimension of c is 0.480 nm, and the angles of α and β are 90° . From the 2D WAXD pattern of the uniaxially oriented amph-7TTF14 film (Fig. 4), it is realized that the TTF groups of amph-7TTF14 self-assemble together to build columns in which the long axis of the column is parallel to the SD. The AA face-to-face stacking fashion of amph-7TTF14 in the self-assembled columns is identified by the (001) and (002) diffractions on the meridian at $2\theta = 18.5^\circ$ and 37.5° . The ($hk1$) diffractions also indicate that each amph-7TTF14 molecule is tilted about 12° with respect to the ab -plane. Careful structural analysis confirms a 3D monoclinic unit cell with dimensions of $a = 2.39$ nm, $b = 4.32$ nm, $c = 0.480$ nm, $\alpha = \beta = 90^\circ$ and $\gamma = 94^\circ$ *via* the refinement of the reciprocal lattice. Therefore, the ordered phase is a highly ordered columnar crystalline phase (abbreviated as the Φ_K phase). The experimentally determined 2θ and d -spacing values are listed in Table 1 on the basis of the unit cell lattice. The crystallographic density calculated from two amph-7TTF14 molecules per unit cell is 0.99 g cm^{-3} , which fits well with the experimentally determined density, *i.e.*, 0.98 g cm^{-3} .

Table 1 Experimental and calculated crystallographic parameters of the monoclinic crystalline (Φ_K) phase of amph-7TTF14

hkl	2θ (deg)		d -spacing (nm)	
	Expt ^a	Calc. ^b	Expt ^a	Calc. ^b
020	4.10	4.10	2.15	2.15
040	8.21	8.21	1.08	1.08
100	3.70	3.70	2.39	2.39
120	5.71	5.71	1.55	1.55
200	7.40	7.40	1.20	1.19
300	11.1	11.1	0.79	0.80
001	18.5	18.5	0.48	0.48
101	18.8	18.9	0.47	0.47
121	19.3	19.4	0.46	0.46
141	20.7	20.7	0.43	0.43
201	20.0	19.9	0.44	0.45
301	21.6	21.6	0.41	0.41
$\bar{3}41$	22.9	22.9	0.39	0.39
401	23.8	23.8	0.38	0.37
501	26.3	26.3	0.34	0.34
002	37.5	37.5	0.24	0.24
102	37.7	37.7	0.23	0.24

^a The accuracy of the experimental data is ± 0.005 nm. ^b The calculated data listed are based on the crystalline (Φ_K) monoclinic unit cell with $a = 2.39$ nm, $b = 4.32$ nm, $c = 0.48$ nm, $\alpha = \beta = 90.0^\circ$ and $\gamma = 94^\circ$.

The existence of columns in the Φ_K crystalline phase is further supported by the TEM morphology and SAED pattern. The bright-field TEM image (inset of Fig. 5a) was taken under the normal conditions for the organic samples.⁵⁷ The bright-field TEM image in Fig. 5a indicates that the morphology of amph-7TTF14 in the Φ_K crystalline phase is similar to cylindrical fibers. Since the onset melting temperature of the Φ_K crystal is close to room temperature, the Φ_K crystals may melt readily even under the normal conditions for TEM morphological observations. To support this speculation, SAED of the cylindrical fiber is conducted. No diffraction is detected because the cylindrical fiber is

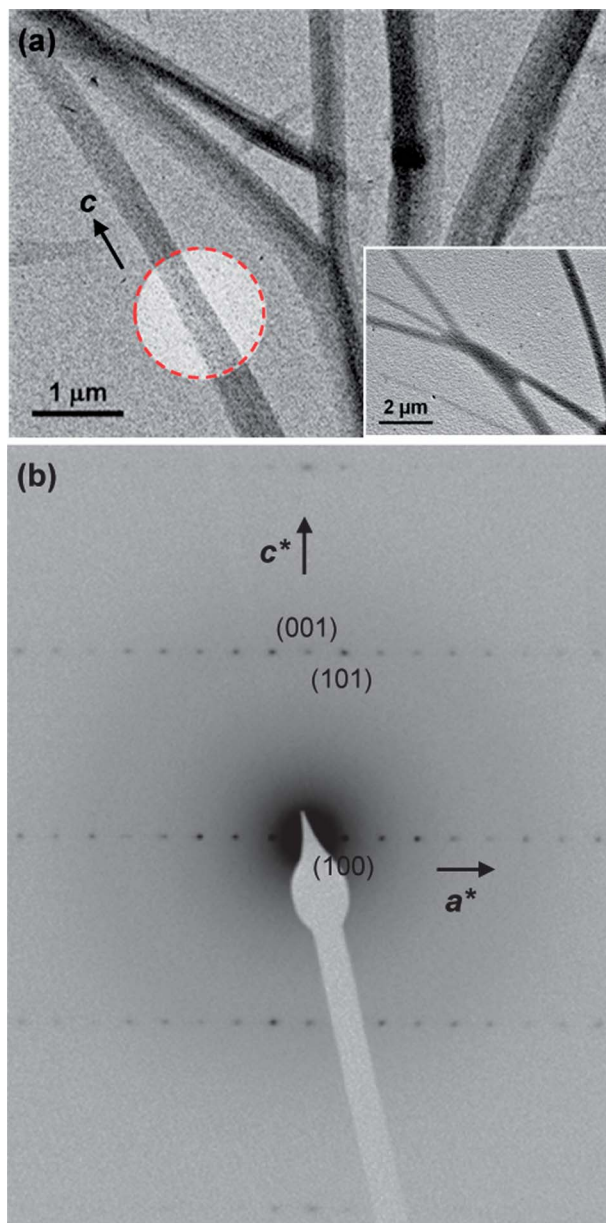


Fig. 5 Bright-field TEM images of the self-assembled amph-7TTF14 flat ribbons with applying a low-dose technique (a). The arrow is pointing along the long axis of the flat ribbons (c -axis). SAED pattern (b) from the circled areas of the bright-field TEM images in part (a). The inset of part (a) is the bright-field TEM image of the self-assembled amph-7TTF14 ribbons taken without applying a low-dose technique.

in disordered and/or decomposed state. In an attempt to get the true crystalline morphology of amph-7TTF14, the melt-crystallized Φ_K crystals are observed under an extremely low dose electron beam radiation. No additional pre-treatments, such as platinum shadowing and polyethylene decoration, are conducted to get rid of any possibilities of melting or decomposition of the crystalline sample during the sample preparation. As shown in Fig. 5a, the amph-7TTF14 compound forms the flat-ribbons rather than the cylindrical fibers.

The SAED pattern of the circular part in Fig. 5a obviously verifies the existence of columns in the flat ribbon crystals, in which the long axes of the flat ribbon and the self-assembled columns are parallel to each other. In Fig. 5b, a pair of strong electron diffraction spots appears at a d -spacing of 2.39 nm, which is close to the (100) diffraction in the 2D WAXD (Fig. 4). The high order diffractions are also well matched with those of the 2D WAXD pattern. Therefore, the a^* -axis is assigned to be along the equator, and the column direction is parallel to the long axis of the flat ribbons which corresponds to the c^* -axis of the Φ_K unit cell. The appearance of (001) diffraction at $2\theta = 18.5^\circ$ (d -spacing = 0.480 nm) on the meridian of 2D WAXD (Fig. 4) is confirmed by the observation of a pair of electron diffraction spots at d -spacing = 0.480 nm on the meridian. Furthermore, the strong (101) diffraction among the series of ($h01$) diffractions supports the fact that TTF groups are tilted about 78° with respect to the long axis of the flat ribbons. Again this result agrees well with that of the 2D WAXD pattern.

Based on the 2D WAXD pattern of the uniaxially oriented film (Fig. 4) and the SAED of the single crystalline flat ribbon (Fig. 5b), the molecular packing in the 3D monoclinic unit cell is proposed, as schematically illustrated in Fig. 6. As discussed in the 2D WAXD pattern, TTF groups of amph-7TTF14 are stacked in the AA face-to-face fashion and form the self-assembled columns. The long axes of columns are parallel to the c -axis, which is normal to the ab -plane (Fig. 6) and parallel to the long axis of the flat ribbon (Fig. 5a). In this molecular packing model, two additional facts should be emphasized. One is the

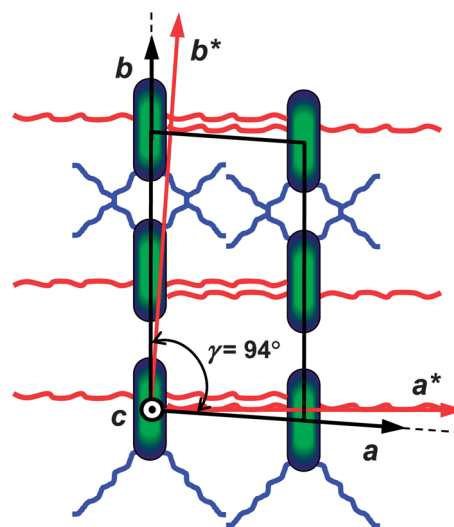


Fig. 6 Schematic illustrations of the amph-7TTF14 molecular arrangements of the flat ribbon on the [001] zone which is normal to the long axis of the flat ribbon.

monoclinic unit cell dimension along the b -axis, and the other is the nanophase separation in the unit cell. In order to reach the thermodynamically stable crystalline state and to compensate the top and bottom surface (ac -plane) stresses of the flat ribbons, the hydrophobic alkyl chains attached to the side of the TTF group and the hydrophilic TEO tails of amph-7TTF14 should be nanophase-separated and TTF groups stack together *via* the π - π interaction. These requirements may be satisfied when the amph-7TTF14 molecule stands in the head-to-head and tail-to-tail fashions along the b -axis on the ab -plane (Fig. 6). As a result, the dimension of the b -axis should be 4.32 nm and the diffraction at $2\theta = 4.10^\circ$ (d -spacing = 2.15 nm) be assigned to (020).

Formation and origin of the scrolled and helical ribbons from achiral amph-7TTF14 compound

A question can be raised at this moment: what happens if the molecules are not in a thermodynamically stable state and remain in a metastable state and thus create the unbalanced surface stresses generated between the flat ribbon basal surfaces? To find an answer for this question, amph-7TTF14 is melt-crystallized from the isotropic phase at various cooling rates (2.5 – $40^\circ\text{C min}^{-1}$). Surprisingly, the scrolled and helical ribbon structures are observed, as represented in Fig. 7a and b, respectively. Upon increasing the cooling rate, the ratio of scrolled and helical ribbon structures is gradually increased but by less than 8% and 2%, respectively. Once these structures are formed during the crystallization process, they do not transform to the flat ribbons even after the annealing process close to the melting temperature. It is considered that the flat ribbon is thermodynamically more stable compared with the scrolled and helical ribbons. The activation barrier blocking the transition from the metastable state (scrolled and helical ribbon) to the stable state (flat ribbon) is high enough so that the scrolled and helical ribbons do not transform to the flat ribbons. The SAED of scrolled ribbons (Fig. S3†) is almost identical to that of the flat one but the diffraction spots are arced and diffused partially due to the scrolled geometry and defects in the ribbons. Therefore, the molecular packing of the scrolled and helical ribbons is almost identical to that of the flat one. Similar to the scrolled and helical ribbons formed in the amphiphilic polymers and small

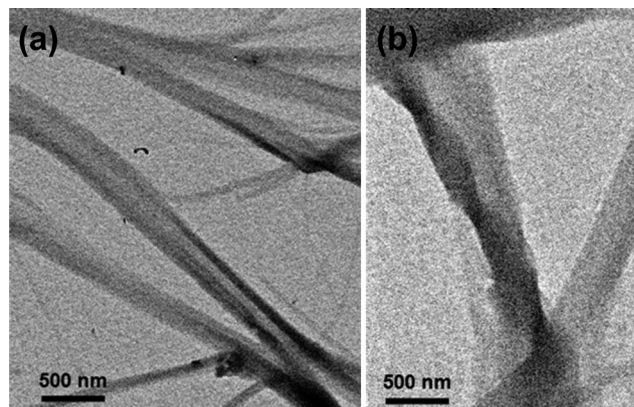


Fig. 7 Bright-field TEM images of the self-assembled amph-7TTF14 ribbons with applying a low-dose technique: scroll (a) and helical (b) ribbons.

organic molecules, the scrolled and helical ribbons of amph-7TTF14 may be induced by the unbalanced surface stresses produced between the basal surfaces of the ribbons. Note that amph-7TTF14 does not contain the configurational chirality but the phase chirality.^{22–37}

The next question is how the unbalanced surface stresses between the basal surfaces of the ribbons can be generated. As schematically illustrated in Fig. 8, the unbalanced surfaces of the ribbons are originated from the molecular packing in the monoclinic unit cell of the crystalline phase. Unlike the flat ribbons, amph-7TTF14 molecules in the scrolled ribbon align to the head-to-tail fashion along the b -axis on the ab -plane (Fig. 8a). Here, the dimension of the b -axis should be 2.15 nm, but the other dimensions of the monoclinic unit cell are maintained. This molecular arrangement still satisfies all the diffraction results from 2D WAXD and SAED. The unbalanced surface stresses between the basal surfaces of the ribbons thereby create the scrolled ribbons. The molecular packing in Fig. 8a gratifies all the main driving forces for the crystallization of amph-7TTF14: the π - π interaction of TTF groups and the nanophase separation among hydrophobic alkyl chains and hydrophilic TEO tails. In addition to the unbalanced surface stresses between the basal surfaces of the ribbons, the helical ribbons of amph-7TTF14 are triggered by the collective tilting of the amph-7TTF14 molecules with respect to the normal direction of the basal plane (b -axis), as illustrated in Fig. 8b. From the bright-field TEM image of the helical ribbons (Fig. 7b), it is found that the twisting power is 20° and helical pitch is 1885 nm. The distance between the neighbouring amph-7TTF14 molecules

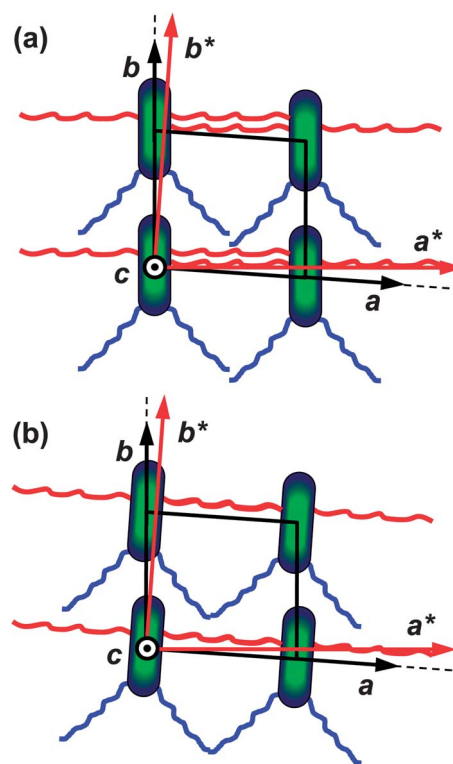


Fig. 8 Schematic illustrations of the amph-7TTF14 molecular arrangements of the scroll (a) and helical (b) ribbons on the [001] zone which is normal to the fast growing direction.

along the long axis of the ribbon (*c*-axis, the long axis of the self-assembled column) is about 0.48 nm, measured by 2D WAXD (Fig. 4). To fill the pitch length of the helical ribbon, about 3928 amph-7TTF14 molecules are continuously tilted around the helical axis. From the 2D WAXD and the TEM image, the local twisting angle from neighbour to neighbour along the long axis of the ribbon is about 0.092° which is on the same order as that of other chiral systems.^{22–37} The proposed molecular packings in Fig. 8 can be elucidated experimentally by the polyethylene (PE) decoration technique combined with the series of SAED patterns obtained by tilting the helical ribbons around the helical axis. However, as demonstrated in the inset of Fig. 5a, the crystalline amph-7TTF14 ribbons are sensitive to the heat generated during the PE decoration and moreover their life time under the electron beam is too short to carry on the tilting experiment.

Construction of macroscopically oriented fibrous hierarchical structures

Surface topology of the crystalline amph-7TTF14 ribbon is investigated by means of AFM. As shown in Fig. 9a, thin ribbons with dimensions of ~ 300 nm width and ~ 20 nm thickness appear and then organize together to make the sheaf of ribbons, which in

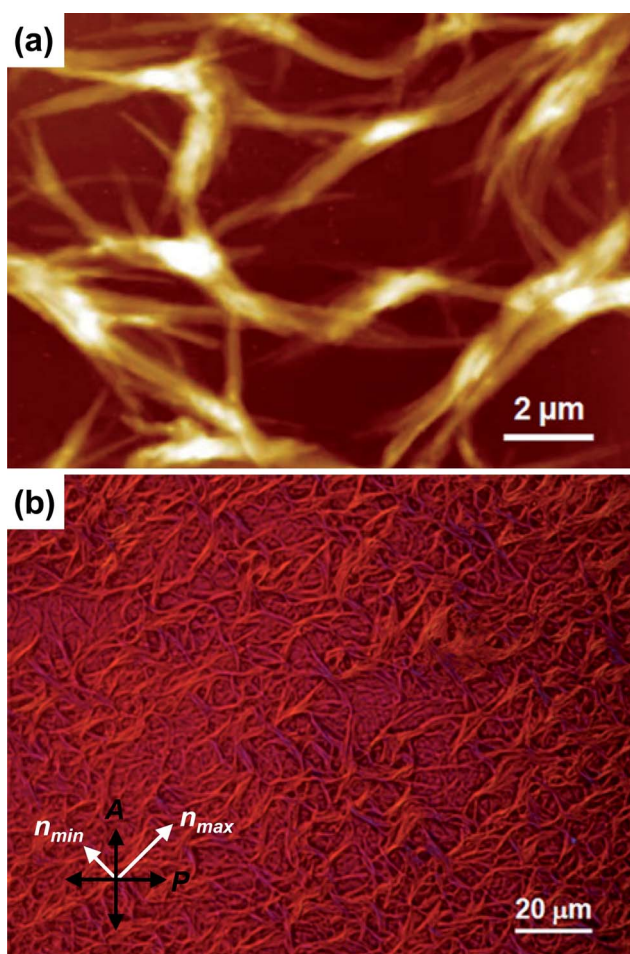


Fig. 9 AFM (a) and POM (b) images of amph-7TTF14 ribbons. A tint retardation film is additionally introduced between the objective lenses and eyepieces for the observation of POM.

turn aggregate to create the fibrous hierarchical structures with various diameters in the micrometer length scale. The fibrous hierarchical structure in the amph-7TTF14 compound is also observed by POM (Fig. 9b). A tint retardation plate (530 nm) was applied between the objective lenses and eyepieces in order to identify the molecular orientation of amph-7TTF14. As depicted in Fig. 9b, when the long axis of the hierarchical fiber is perpendicular to the n_{\max} (the slow direction) of the tint retardation plate, the colour of the fiber is bluish, while the rest of the area looks yellowish. Note that the POM image of the disordered sample is reddish under a tint retardation plate. This textural observation supports the results in 2D WAXD, TEM, SAED and AFM studies. The amph-7TTF14 molecules self-assemble to columns and the columns self-organize to ribbons and the ribbons aggregate side-by-side to form the hierarchical fibers, as schematically illustrated in Fig. 10. Therefore, the long axis of the TTF group is parallel to the n_{\max} (the slow direction) which is perpendicular to the long axis of the fiber. To support this explanation and to attempt to align the hierarchical fibers, the amph-7TTF14 thin film is heated close to the onset melting temperature and then mechanically sheared between the two bare glasses. The POM image shown in Fig. 11a reveals that the hierarchical fibers with the average diameter of $1.5 \mu\text{m}$ are macroscopically aligned parallel to the shear direction (SD) and form an anisotropic film. As expected, the hierarchical fibers aligned parallel to the SD (n_{\min} , the fast direction) show a bluish colour (Fig. 11b). The long axis of the TTF group in the amph-7TTF14 molecule should be perpendicular to the long axis of the fiber and parallel to the n_{\max} (the slow direction). When the anisotropic amph-7TTF14 films consisted of the fibrous hierarchical structure are properly applied to the electrooptical and bio-mimetic devices, the targeted physical properties may be significantly improved and tuned for the specific practical applications.

Optical and electrical properties of amph-7TTF14 compound

The optical properties of the amph-7TTF14 compound are also investigated using UV-Vis spectroscopy (Fig. S4†) and summarized in Table 2. The maximum absorption peak of the amph-7TTF14 compound in chloroform appears at around 384 nm and the optical band gap energy (E_g) is 2.73 eV from the absorption tail. The optical band gap energy of the amph-7TTF14 compound is higher than that of pentacene (2.2 eV), suggesting a better air stability.^{58–67} The amph-7TTF14 compound is chemically oxidized in dichloromethane solution (*ca.* 2×10^{-5} M) by a stepwise addition of FeCl_3 to explore the electronic transferring behaviour and then the variation of UV-Vis absorption spectra is

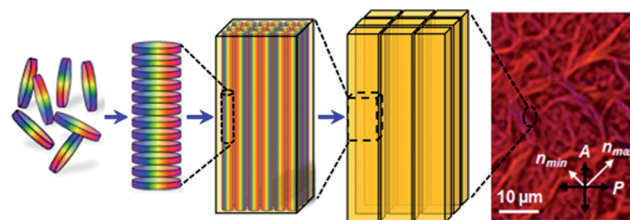


Fig. 10 Schematic illustration of the self-assembly and self-organization process of amph-7TTF14.

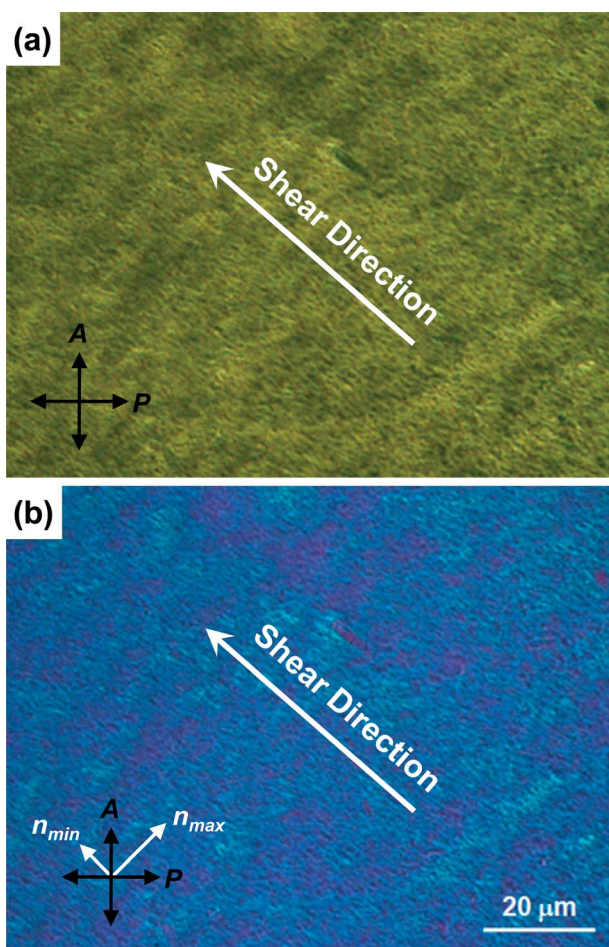


Fig. 11 POM images of the oriented amph-7TTF14 ribbons with (a) and without (b) a tint retardation film between the objective lenses and eyepieces.

also monitored (Fig. S5†). The absorption bands at 469 and 807 nm newly appear concomitantly and the intensity and area increase as oxidation proceeds. The absorption at 469 nm is ascribed to the intramolecular electron transfer of the radical cation, while the absorption band at 807 nm is due to the intermolecular electron transfer of the dicationic π -dimers. The mechanically oriented amph-7TTF14 film is examined using linear polarized UV-Vis spectroscopy (Fig. S6†). Absorption maximum of the amph-7TTF14 solid film is red-shifted, which is slightly different from that of amph-7TTF14 in solution. It may

Table 2 Optical, electrochemical potentials and energy levels of amph-7TTF14

	E_1^a (V)	E_2^a (V)	UV (nm)	E_g^b (eV)	HOMO ^c (eV)
TTF	0.34 ^d	0.73 ^d	—	—	—
amph-7TTF14	0.89	1.20	384	2.73	-5.23

^a E_1 and E_2 mean the half wave oxidation potentials. ^b $E_g = hc/\lambda_{0.1\max}$. E_g means the optical band gap energy. $\lambda_{0.1\max}$ means the wavelength at which the absorption coefficient drops to 10% of the peak value.⁶⁵ ^c $E_{\text{HOMO}} = -(E_{\text{onset}}^{\text{ox}} + 4.4 \text{ eV})$, where $E_{\text{onset}}^{\text{ox}}$ is the onset potential for the oxidation.⁶⁶ ^d From ref. 67.

be attributable to the π - π interactions between TTF groups in the self-assembled amph-7TTF14 columns. With increasing the angle between the polarizer and SD from 0° to 90° , the absorption intensity at 409 nm increases, indicating that the long axis of the TTF group is perpendicular to the fiber direction. This conclusion is well matched with the results obtained from 2D WAXD, SAED and POM.

The electrochemical property of the amph-7TTF14 compound is also studied using CV. The CV measurements are performed in a dry dichloromethane solution of Bu_4NBF_4 (0.1 M) with a scan rate of 100 mV s^{-1} at room temperature (Fig. S7†). The results are tabulated in Table 2. The amph-7TTF14 compound exhibits two irreversible single-electron oxidation peaks at 0.89 and 1.20 V which correspond to the radical cations and dications, respectively. Both oxidation potentials of amph-7TTF14 are higher than those of the pristine TTF molecules presumably due to the electron-withdrawing ester linkages.

Experimental

Materials and sample preparations

For 1D WAXD measurements, film samples with a thickness of about 1 mm were prepared by melting the amph-7TTF14 compound on an aluminium plate. To determine the phase structure of amph-7TTF14 using 2D WAXD, the oriented samples with a thickness of about 0.2 mm were prepared by mechanical shearing at the phase transition temperature between the isotropic and ordered crystalline phases. The uniaxially oriented amph-7TTF14 samples were also utilized for the polarized UV-Vis spectroscopy and cross-polarized POM experiments. The samples for POM were melt-processed between two bare cover glass slides to form a thin film ($\sim 10 \mu\text{m}$ thickness). For TEM and AFM analyses, the thin film (50–150 nm) was prepared by dropping 0.05% (w/v) tetrahydrofuran solution onto carbon-coated mica. After evaporating the solvent, the carbon films were floated on a water surface and then recovered using TEM copper grids. After the melt crystallization, no additional treatments were carried out for the TEM observation.

Equipment and experiments

The thermal behaviour of amph-7TTF14 molecules was monitored using a Perkin-Elmer PYRIS Diamond DSC equipped with an Intracooler 2P apparatus. The temperatures and heat flows were calibrated using standard materials at the cooling/heating rates of $2.5\text{--}40 \text{ }^\circ\text{C min}^{-1}$. Heating scans always preceded the cooling scans at the same rate to eliminate the previous thermal histories. The transition temperatures were determined by measuring the onset temperatures obtained during the cooling and heating scans at different rates.

1D WAXD experiments were conducted in the reflection mode of a Rigaku 12 kW rotating-anode X-ray (Cu $K\alpha$ radiation) generator coupled with a diffractometer. The diffraction peak positions and widths were calibrated with silicon crystals in the high 2θ -angle region ($>15^\circ$) and silver behenate in the low 2θ -angle region. To monitor the structural evolutions with temperature changes, a hot stage calibrated to be within $\pm 1 \text{ }^\circ\text{C}$ error was coupled to the diffractometer. Samples were scanned across a 2θ -angle range of 1.5° to 35° at a scanning rate of 2 deg

min⁻¹. The 2D WAXD patterns were obtained using a Rigaku X-ray imaging system with an 18 kW rotating anode X-ray generator. Silicon crystal powder, used as an internal reference, shows a diffraction ring at a 2θ value of 28.466°. For the 2D WAXD experiment, at least 30 min of exposure time was required for a high-quality pattern. In both 1D and 2D WAXD experiments, background scattering was subtracted from the sample scans.

Bright-field TEM images (FEI Tecnai 12) were taken to examine the film morphology on the nanometer length scale at an accelerating voltage of 120 kV. The camera length for SAED analysis was set at 3.0 m, and the calibration of the SAED spacing smaller than 0.384 nm was carried out using evaporated thallos chloride, which has a largest first-order spacing diffraction of 0.384 nm. Spacing values larger than 0.384 nm were calibrated by doubling the d -spacing values of the first-order diffractions.

An AFM (Digital Instrument, Nanoscope IIIa) technique was employed to investigate the surface topology of the amph-7TTF14 ribbons. To get the height images, the contact mode with a 100 μm scanner was applied. The force used by the cantilever was light enough to prevent the unexpected damage, but sufficient to accurately explore the surface features. The scanning rate was manipulated to be 1–3 Hz for the low-magnification images. The data were collected with the 512×512 pixels per image resolution.

The change of optical textures at a given temperature was observed using cross-polarized POM (Nikon ECLIPSE E600POL) coupled with a LINKAM LTS 350 heating stage. A tint retardation plate (530 nm) was additionally placed between the objective lenses and the eyepieces in order to identify the molecular orientation in the POM textures.

¹H and ¹³C NMR spectra were recorded on a JNM-EX400 spectrometer in deuterated chloroform. Chemical shifts were quoted in parts per million (ppm) and referenced to tetramethylsilane. UV-Vis absorption spectra were obtained with a SCINCO S-3100 spectrometer. CV measurements were performed by Versa STAT3 of Princeton Applied Research in a solution of Bu₄NBF₄ (0.1 M in water-free dichloromethane) with a scan rate of 100 mV s⁻¹ at room temperature. A glass carbon electrode, a Ag/AgCl electrode and a platinum wire were used as the working electrode, the reference electrode and the counter electrode, respectively.

Conclusions

An achiral amphiphilic tetrathiafulvalene (TTF) molecule (amph-7TTF14) containing two tri(ethylene oxide) tails and two alkyl chains with 14 carbons at the end and side of the asymmetric TTF group was newly designed and synthesized. On the basis of the combined DSC, 1D/2D WAXD and SAED techniques, it was realized that the amph-7TTF14 compound formed a highly ordered monoclinic crystal (Φ_K) with dimensions of $a = 2.39$ nm, $b = 4.32$ nm, $c = 0.480$ nm, $\alpha = \beta = 90^\circ$ and $\gamma = 94^\circ$. The governing forces for the self-assembly of amph-7TTF14 were the face-to-face π - π interaction among TTF groups and the nanophase separation between rigid TTF groups and flexible hydrophobic alkyl and hydrophilic tri(ethylene oxide) tails. The morphological observations using

TEM, AFM, and POM techniques indicated that the amph-7TTF14 compound formed not only flat ribbons but also scrolled and helical ribbons. The self-assembled ribbons further aggregated themselves to create the fibrous hierarchical structures with various diameters in the micrometer length scale. The scrolled and helical ribbon structures are induced by the unbalanced surface stresses generated during the crystallization process. The molecular orientation of the macroscopically oriented amph-7TTF14 film consisting of the hierarchical fibers was further confirmed using POM with a retardation film. The outstanding optical and electrochemical properties of amph-7TTF14 may provide promising opportunities for organic optoelectronic devices.

Acknowledgements

This work was mainly supported by the Ministry of Education, Science Technology through the Human Resource Training Project for Regional Innovation, Basic Science Research Program (2011-0004900) and Converging Research Center Program (2011K000776), Korea.

Notes and references

- 1 G. Sun and C.-C. Chu, *ACS Nano*, 2009, **3**, 1176.
- 2 M. J. Molla and S. Ghosh, *Chem. Mater.*, 2011, **23**, 95.
- 3 J.-R. Gong, S.-B. Lei, L.-J. Wan, G.-J. Deng, Q.-H. Fan and C.-L. Bai, *Chem. Mater.*, 2003, **15**, 3098.
- 4 X. Dou, G. Li and H. Lei, *Nano Lett.*, 2008, **8**, 1286.
- 5 H. Shen, K.-U. Jeong, H. Xiong, M. J. Graham, S. Leng, J. X. Zheng, H. Huang, M. Guo, F. W. Harris and S. Z. D. Cheng, *Soft Matter*, 2006, **2**, 232.
- 6 S. Leng, L. H. Chan, J. Jing, J. Hu, R. M. Moustafa, R. M. Van Horn, M. J. Graham, B. Sun, M. Zhu, K.-U. Jeong, B. R. Kaafarani, W. Zhang, F. W. Harris and S. Z. D. Cheng, *Soft Matter*, 2010, **6**, 100.
- 7 H.-J. Sun, C.-L. Wang, I.-F. Hsieh, C.-H. Hsu, R. M. Van Horn, C.-C. Tsai, K.-U. Jeong, B. Lotz and S. Z. D. Cheng, *Soft Matter*, 2012, **8**, 4767.
- 8 Y.-H. Ye, T. S. Mayer, I.-C. Khoo, I. B. Diclansky, N. Abrams, T. E. Mallouk, J. H. Jeon and H. Hidai, *J. Mater. Chem.*, 2002, **12**, 3637.
- 9 G. Shen, Y. Bando and D. Golberf, *Cryst. Growth Des.*, 2007, **7**, 35.
- 10 M. Kastler, W. Pisula, F. Laquai, A. Kumar, R. J. Davies, S. Baluschev, M.-C. Garcia-Gutiérrez, D. Wasserfallen, J.-J. Butt, C. Riekel, G. Wegner and K. Müllen, *Adv. Mater.*, 2006, **18**, 2255.
- 11 J.-L. Mi, N. Lock, T. Sun, M. Christensen, M. Sondergaard, P. Hald, H. H. Hng, J. Ma and B. B. Iverson, *ACS Nano*, 2010, **4**, 2523.
- 12 I. M. Saez and J. W. Goodby, *J. Mater. Chem.*, 2005, **15**, 26.
- 13 D. Stamenovic and D. E. Ingber, *Soft Matter*, 2009, **5**, 1137.
- 14 R. S. Tu, R. Marullo, R. Pynn, R. Bitton, H. Bianco-Peled and M. W. Tirrell, *Soft Matter*, 2010, **6**, 1035.
- 15 S. M. Yu, Y. Li and D. Kim, *Soft Matter*, 2011, **7**, 7927.
- 16 L. Zhou, J. Ye, G. Hong and L. Qi, *Soft Matter*, 2011, **7**, 9624.
- 17 G. Zubay, *Biochemistry*, Macmillan Publishing Company, New York, 2nd edn, 1988, pp. 845–1151.
- 18 S. Keinan and D. Avnir, *J. Am. Chem. Soc.*, 1998, **120**, 6152.
- 19 N. P. Chmel, G. J. Clarkson, A. Troisi, S. S. Turner and P. Scott, *Inorg. Chem.*, 2011, **50**, 4039.
- 20 M. Segura, L. Sánchez, J. de Mendoza, N. Martin and D. M. Guldi, *J. Am. Chem. Soc.*, 2003, **125**, 15093.
- 21 C. Bombis, S. Weigelt, M. M. Knudsen, M. Nørgaard, C. Busse, E. Lægsgaard, F. Besenbacher, K. V. Gothelf and T. R. Linderth, *ACS Nano*, 2010, **4**, 297.
- 22 C. Y. Li, D. Yan, S. Z. D. Cheng, F. Bai, T. He, L. C. Chien, F. W. Harris and B. Lotz, *Macromolecules*, 1999, **32**, 524.
- 23 C. Y. Li, D. Yan, S. Z. D. Cheng, F. Bai, J. J. Ge, B. H. Calhoun, T. He, L. C. Chien, R. W. Harris and B. Lotz, *Phys. Rev. B: Condens. Matter*, 1999, **60**, 12675.

- 24 C. Y. Li, D. Yan, S. Z. D. Cheng, J. J. Ge, F. Bai, J. Z. Zhang, I. K. Mann, F. W. Harris, L. C. Chien, D. Yan, T. He and B. Lotz, *Phys. Rev. Lett.*, 1999, **83**, 4558.
- 25 C. Y. Li, J. J. Ge, F. Bai, J. Z. Zhang, B. H. Calhoun, L. C. Chien, F. W. Harris, B. Lotz and S. Z. D. Cheng, *Polymer*, 2000, **41**, 8953.
- 26 C. Y. Li, S. Z. D. Cheng, J. J. Ge, F. Bai, J. Z. Zhang, I. K. Mann, L. C. Chien, F. W. Harris and B. Lotz, *J. Am. Chem. Soc.*, 2000, **122**, 72.
- 27 C. Y. Li, S. Z. D. Cheng, X. Weng, J. J. Ge, F. Bai, J. Z. Zhang, B. H. Calhoun, F. W. Harris, L. C. Chien and B. Lotz, *J. Am. Chem. Soc.*, 2001, **123**, 2462.
- 28 C. Y. Li, J. J. Ge, R. Bai, B. H. Calhoun, F. W. Harris, S. Z. D. Cheng, L. C. Chien, B. Lotz and H. D. Keith, *Macromolecules*, 2001, **34**, 3634.
- 29 C. Y. Li, S. Jin, X. Weng, J. J. Ge, D. Zhang, R. Bari, R. W. Harris, S. Z. D. Cheng, D. Yan, T. He, B. Lotz and L. C. Chien, *Macromolecules*, 2002, **35**, 5475.
- 30 X. Weng, C. Y. Li, S. Jin, J. J. Zhang, D. Zhang, F. W. Harris, S. Z. D. Cheng and B. Lotz, *Macromolecules*, 2002, **35**, 9678.
- 31 D. R. Link, G. Natale, R. Shao, J. E. McLennan, N. A. Clark, E. Korblova and D. M. Walba, *Science*, 1997, **278**, 1924.
- 32 S. Kobayashi, N. Hamsaki, M. Suzuki, M. Kimura, H. Shirai and K. Hanbusa, *J. Am. Chem. Soc.*, 2002, **124**, 6560.
- 33 W. Yang, X. Chai, L. Chi, X. Liu, Y. Cao, R. Lu, Y. Jiang, X. Tang, H. Fuchs and T. Li, *Chem.-Eur. J.*, 1999, **5**, 1144.
- 34 J. H. Hirschberg, L. Brunsveld, A. Ramzi, J. A. Vekemans, R. P. Sijbesma and E. W. Meijer, *Nature*, 2000, **407**, 167.
- 35 D. N. Reinhoudt and M. Drego-Clalma, *Science*, 2002, **295**, 2403.
- 36 I. Miyake, Y. Takamishi, N. V. S. Rao, M. Kr. Paul, K. Ishikawa and H. Takezoe, *J. Mater. Chem.*, 2005, **15**, 4688.
- 37 S. Jin, Y. Ma, S. C. Zimmerman and S. Z. D. Cheng, *Chem. Mater.*, 2004, **16**, 2975.
- 38 L. Wang, K.-U. Jeong and M.-H. Lee, *J. Mater. Chem.*, 2008, **18**, 2657.
- 39 Naraso, J. Nishida, S. Ando, J. Yamaguchi, K. Itaka, H. Koinuma, H. Tada, S. Tokito and Y. Yamashita, *J. Am. Chem. Soc.*, 2005, **127**, 10142.
- 40 J. Casado, M. Z. Zgierski, D. M. C. Ruiz, N. J. T. Lopez, M. Mas-Torrent and C. Rovira, *J. Phys. Chem. C*, 2007, **111**, 10110.
- 41 G. Ungar, J. L. Feijoo, V. Percec and R. Yourd, *Macromolecules*, 1991, **24**, 953.
- 42 M. A. Yandrasits, S. Z. D. Cheng, A. Zhang, J. Cheng, B. Wunderlich and V. Percec, *Macromolecules*, 1992, **25**, 2112.
- 43 R. Pardey, A. Zhang, P. A. Gabori, F. W. Harris, S. Z. D. Cheng, J. Adduci, J. V. Facinelli and R. W. Lenz, *Macromolecules*, 1992, **25**, 5060.
- 44 R. Pardey, D. Shen, P. A. Gabori, F. W. Harris, S. Z. D. Cheng, J. Adduci, J. V. Facinelli and R. W. Lenz, *Macromolecules*, 1993, **26**, 3687.
- 45 Y. Yoon, A. Zhang, R.-M. Ho, S. Z. D. Cheng, V. Percec and P. Chu, *Macromolecules*, 1996, **29**, 294.
- 46 Y. Yoon, R.-M. Ho, B. Moon, D. Kim, K. W. McCreight, F. Li, F. W. Harris, S. Z. D. Cheng, V. Percec and P. Chu, *Macromolecules*, 1996, **29**, 3421.
- 47 R.-Q. Zheng, E.-Q. Chen and S. Z. D. Cheng, *Macromolecules*, 1999, **32**, 3574.
- 48 R.-Q. Zheng, E.-Q. Chen, S. Z. D. Cheng, F. Xie, D. Yan, T. He, V. Percec, P. Chu and G. Ungar, *Macromolecules*, 1999, **32**, 6981.
- 49 K.-U. Jeong, S. Jin, J. J. Ge, B. S. Knapp, M. J. Graham, J. Ruan, M. Guo, H. Xiong, F. W. Harris and S. Z. D. Cheng, *Chem. Mater.*, 2005, **17**, 2852.
- 50 K.-U. Jeong, B. S. Knapp, J. J. Ge, S. Jin, M. J. Graham, H. Xiong, F. W. Harris and S. Z. D. Cheng, *Macromolecules*, 2005, **38**, 8333.
- 51 K.-U. Jeong, B. S. Knapp, J. J. Ge, S. Jin, M. J. Graham, F. W. Harris and S. Z. D. Cheng, *Chem. Mater.*, 2006, **18**, 680.
- 52 K.-U. Jeong, B. S. Knapp, J. J. Ge, M. J. Graham, Y. Tu, S. Leng, H. Xiong, F. W. Harris and S. Z. D. Cheng, *Polymer*, 2006, **47**, 3351.
- 53 K.-U. Jeong, D. K. Yang, M. J. Graham, Y. Tu, S. W. Kuo, B. S. Knapp, F. W. Harris and S. Z. D. Cheng, *Adv. Mater.*, 2006, **18**, 3229.
- 54 D.-K. Yang, K.-U. Jeong and S. Z. D. Cheng, *J. Phys. Chem. B*, 2008, **112**, 1358.
- 55 K.-U. Jeong, A. J. Jing, B. Monsdorf, J. Matthew, R. W. Harris and S. Z. D. Cheng, *J. Phys. Chem. C*, 2007, **111**, 767.
- 56 L. Wang, S.-J. Park, S.-H. Lee, Y.-J. Kim, Y.-B. Kook, S.-W. Kuo, R. M. Van Horn, S. Z. D. Cheng, M.-H. Lee and K.-U. Jeong, *Chem. Mater.*, 2009, **21**, 3838.
- 57 S. Jin, K.-U. Jeong, Y. Tu, M. J. Graham, J. Wang, F. W. Harris and S. Z. D. Cheng, *Macromolecules*, 2007, **40**, 5450.
- 58 M. Yoshizawa, K. Kumazawa and M. Fujita, *J. Am. Chem. Soc.*, 2005, **127**, 13456.
- 59 J. Xiao, Z. Yin, H. Li, Q. Zhang, F. Boey, H. Zhang and Q. Zhang, *J. Am. Chem. Soc.*, 2010, **132**, 6926.
- 60 R. Yuge, A. Miyazaki, T. Enoki, K. Tamada, F. Nakamura and M. Hara, *J. Phys. Chem. B*, 2002, **106**, 6894.
- 61 C. Bellitto, M. Bonamico, V. Fares and P. Serino, *Inorg. Chem.*, 1996, **35**, 4070.
- 62 S. Currli, P. Deplano, M. L. Mercuri, L. Pilia, A. Serpe, A. John, A. S. Micheal, G. W. Urs, E. Coronado, C. J. Gómez-García and E. Canadell, *Inorg. Chem.*, 2004, **43**, 2059.
- 63 N. Dupont, Y.-F. Ran, H.-P. Jia, J. Grilj, J. Ding, S.-X. Lui, S. Decurtins and A. Hauser, *Inorg. Chem.*, 2011, **50**, 3295.
- 64 A. Decken, T. S. Cameron, J. Passmore, J. M. Rautiainen, R. W. Reed, K. V. Shuvaev and L. K. Thompson, *Inorg. Chem.*, 2007, **46**, 7436.
- 65 D. A. M. Egbe, C. Bader, J. Nowotny, W. Günther and E. Klemm, *Macromolecules*, 2003, **36**, 5459.
- 66 D. D. M. Leeuw, M. M. J. Simenon, A. R. Brown and R. E. F. Einerhand, *Synth. Met.*, 1997, **87**, 53.
- 67 J. O. Jeppesen, K. Takimiya, F. Jensen, T. Brimert, K. Nielsen, N. Thorup and J. Becher, *J. Org. Chem.*, 2000, **65**, 5794.